

Forensic analysis of rockfall scars

1
2
3
4
5
6
7
8
9
10
11
12
13
14
15
16
17
18
19
20
21

de Vilder, S.J.^{1*}, Rosser, N.J.¹, Brain, M.J.¹

¹Department of Geography, Durham University, Lower Mountjoy, South Road, Durham DH1
3LE UK

*Corresponding author: s.j.de-vilder@durham.ac.uk

Keywords: Rock bridges, Failure mechanisms, Rock mass strength, Discontinuity
persistence, Rockslope failures, Progressive failure.

22 **Abstract:**

23 We characterise and analyse the detachment (scar) surfaces of rockfalls to understand the
24 mechanisms that underpin their failure. Rockfall scars are variously weathered and
25 comprised of both discontinuity release surfaces and surfaces indicative of fracturing through
26 zones of previously intact rock, known as rock bridges. The presence of rock bridges and
27 pre-existing discontinuities is challenging to quantify due to the difficulty in determining
28 discontinuity persistence below the surface of a rock slope. Rock bridges form an important
29 control in holding blocks onto rockslopes, with their frequency, extent and location commonly
30 modelled from the surface exposure of daylighting discontinuities. We explore an alternative
31 approach to assessing their role, by characterising failure scars. We analysed a database of
32 multiple rockfall scar surfaces detailing the areal extent, shape, and location of broken rock
33 bridges and weathered surfaces. Terrestrial laser scanning and gigapixel imagery were
34 combined to record the detailed texture and surface morphology. From this, scar surfaces
35 were mapped via automated classification based on RGB pixel values.

36 Our analysis of the resulting data from scars on the North Yorkshire coast (UK) indicates a
37 wide variation in both weathering and rock bridge properties, controlled by lithology and
38 associated rock mass structure. Importantly, the proportion of rock bridges in a rockfall
39 failure surface does not increase with failure size. Rather larger failures display fracturing
40 through multiple rock bridges, and in contrast smaller failures fracture occurs only through a
41 single critical rock bridge. This holds implications for how failure mechanism changes with
42 rockfall size and shape. Additionally, the location of rock bridges with respect to the
43 geometry of an incipient rockfall is shown to determine failure mode. Weathering can occur
44 both along discontinuity surfaces and previously broken rock bridges, indicating the
45 sequential stages of progressively detaching rockfall. Our findings have wider implications
46 for hazard assessment where rock slope stability is dependent on the nature of rock bridges,
47 how this is accounted for in slope stability modelling, and the implications of rock bridges on
48 long-term rock slope evolution.

49 1. Introduction

50 The scar left behind after a rockfall from a rock face, commonly comprised of exposed joint
51 surfaces separated by zones of broken intact rock termed *rock bridges*, holds significant
52 insights into the conditions prior to failure, and the mechanics of that failure. Despite this, the
53 analysis of failure scars has been largely restricted to detailed post-failure analysis of single,
54 commonly large, rockfall or rockslides, rather than analysis of an inventory of multiple events
55 (e.g. Frayssines and Hantz, 2006; Paronuzzi and Sera, 2009; Sturzenegger and Stead,
56 2012). To gain insight into the influence of rock structure on stability, failure mechanisms are
57 commonly inferred from the back analysis of stability based upon the wider slopes' rock
58 mass strength (RMS), which is estimated from the combined influence of pre-existing
59 discontinuities, intact rock strength, and the degree of weathering (Barton, 1974; Hoek and
60 Brown, 1997; Jennings, 1970; Selby, 1980). The control of intact rock strength is most
61 significant at rock bridges, as they form the attachment points holding a failing block to the
62 rock mass (Jennings, 1970) (Figure 1a). Failure is known to often occur as a complex, time-
63 dependent interaction between shearing along discontinuities and progressive fracturing
64 through rock bridges, termed 'step-path' failure (Brideau et al., 2009; Jennings, 1970;
65 Scavia, 1995).

66 Structural assessment of stability is routinely undertaken through field investigation by direct
67 observation (e.g. Priest, 1993), remote sensing (e.g. Dunning et al., 2009; Sturzenegger and
68 Stead, 2009), geophysical survey (e.g. Clarke and Burbank, 2011), or intrusive ground
69 investigations such as borehole logging. However, characterising the persistence of
70 discontinuities through a potentially unstable rock slope remains challenging. As such, many
71 studies have assumed that discontinuities are fully persistent and the resulting stability
72 analysis employs a purely kinematic analysis of failure (e.g. Goodman and Shi, 1985; Wyllie
73 and Mah, 2004). Importantly however, rock bridges influence overall slope stability, and
74 experiments with limit equilibrium modelling shows even a single-digit percentage presence
75 of rock bridges as a proportion of total discontinuity length within a slope will substantially

76 increase the overall factor of safety (Frayssines and Hantz, 2009; Jennings, 1970). Field
77 data from previous failures suggests a wide range in a rock bridge prevalence that is
78 inevitably site specific, including very small percentages (0.2% to 45% as reported by:
79 Tuckey and Stead, 2016 and references therein). In addition, prior to failure the slope can
80 become weakened via a complex suite of weathering processes (Viles, 2013), which alter
81 the mechanical properties of exposed discontinuities, already broken rock bridges and those,
82 which may break in future.

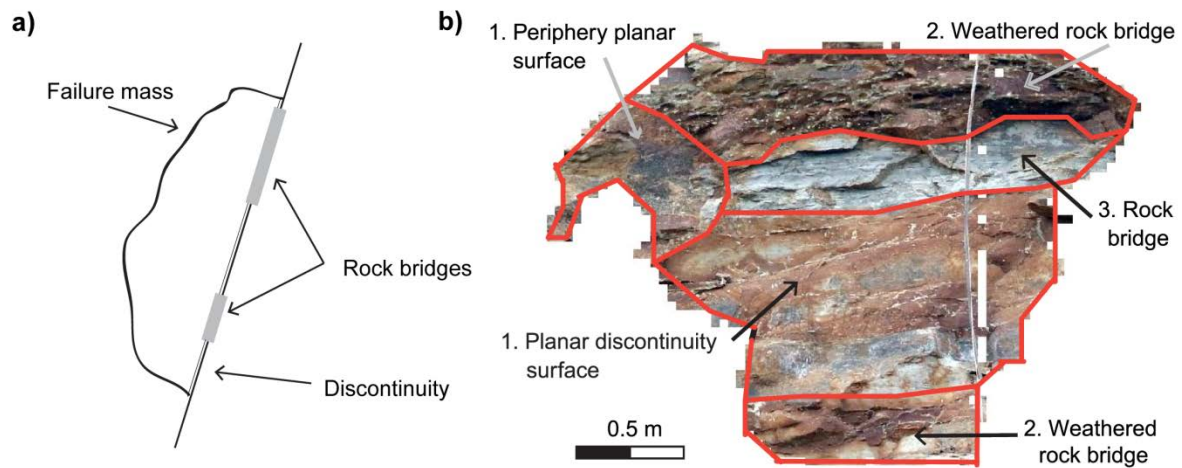
83 The identification and attributes of significant intact rock bridges is poorly constrained in field
84 studies, due to the difficulty of assessing their presence within the rock mass. Forensic
85 analysis of a rockfall scar provides the most direct assessment of their role within a rockfall
86 event (Figure 1b). However, few studies have fully characterised rockfall scars, with many
87 focussed on specific analysis at single sites. This, combined with the wide range of reported
88 rock bridge presence and only limited and disparate assessment of general characteristics
89 between sites, we argue provides insufficient evidence to fully constrain the role of rock
90 bridges in controlling rockfall (e.g. Frayssines and Hantz, 2006; Lévy et al., 2010; Paronuzzi
91 et al., 2016).

92 A broader assessment, and detailed analysis of both rock bridges and other scar attributes
93 can be used to infer the nature of stresses at the time of failure (e.g. Paronuzzi et al., 2016;
94 Paronuzzi and Sera, 2009), subsequent failure mode (Bonilla-Sierra et al., 2015; Stock et al.,
95 2011), the sequence of rock bridge breakage (Stock et al., 2012), and the prevalence of
96 weathering, and hence relative age of discontinuities and rock bridge breakage. This has
97 important implications for hazard assessment of individual slopes (Fell et al., 2008), and also
98 for how rock strength and structure influence longer-term landform change (Clarke and
99 Burbank, 2010; Koons et al., 2012).

100 To address this, we present analysis of a rockfall scar database consisting of 657 individual
101 rockfalls, which range in surface area from 0.1 m² to 27 m². Our aim is to characterise rock

102 bridges within individual rockfall scars in this inventory in order to understand how they
103 determine the type, mode and location of failure.

104



105

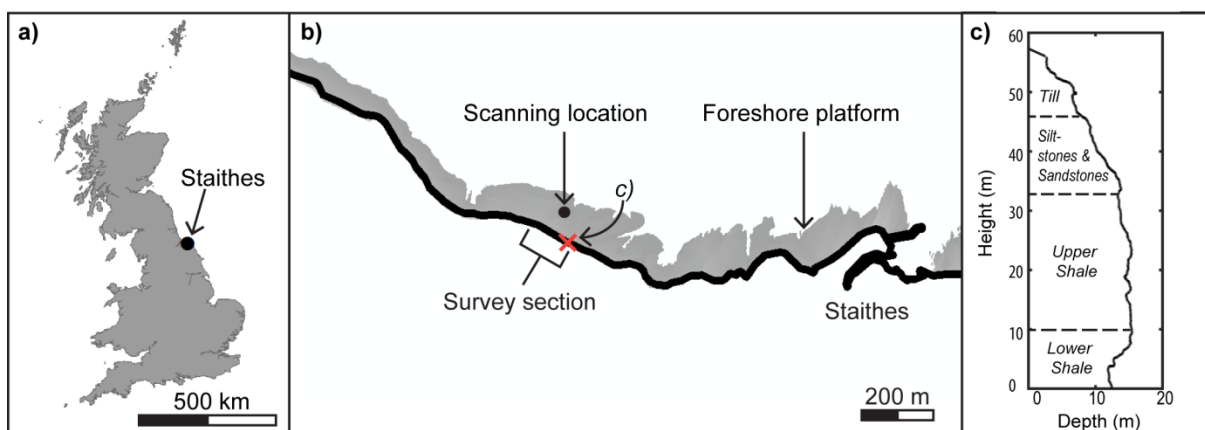
106 Figure 1: a) Simplified profile view of a rockfall held to a rockslope by rock bridges and a pre-
107 existing yet not fully formed discontinuity. The incipient rockfall requires the rock bridges
108 separating the discontinuities to be broken before failure can occur. b) Example high
109 resolution photograph of a siltstone rockfall scar, from North Yorkshire coastal cliffs, U.K.
110 The scar contains discontinuities of varying persistence, plus three separate broken rock
111 bridges that have been variously weathered, as indicated by the surface colour. Analysis of
112 the age of the features, as indicated by their weathering, suggests the order of failure, with
113 the discontinuity surfaces forming first, before fracturing and weathering of rock bridges, and
114 the final fracture of a freshly exposed rock bridge.

115

116 2. Study Site

117 We monitored a 200 m section of near-vertical cliffs at Staithes, North Yorkshire, UK over a
118 13-month period to document and characterise rockfall activity (Figure 2). The rock portion of
119 the cliffs is ~60 m in height, and located on a storm-dominated macro-tidal coastal

120 environment. The 200 m survey section contains a lower shale unit (~10 m high, extending
 121 from the cliff toe at mean high water level), an upper shale unit (~32 m high) and an
 122 interbedded siltstone and sandstone unit (~12 m high), capped by a glacial till (Figure 2c).
 123 These form part the of the Lower Jurassic Redcar Mudstone and Staithes Sandstone
 124 formations (Rawson and Wright, 2000). All units display a bedding dip of 2° to the south-
 125 east, which is broadly orthogonal to the northern aspect of the cliff face, and a complex
 126 discontinuity pattern, which varies in orientation and persistence between the interbedded
 127 layers in each major rock type. From field mapping, the dark blue-grey lower shale unit is
 128 slightly weathered with some surficial algal cover, is moderately strong to strong, and has
 129 indistinct bedding with iron-stone bands throughout, as well as a widely spaced joint pattern
 130 of varying persistence (classification based on ISRM, 2015). The upper shale unit is similar
 131 with a dark blue-grey colouring, slightly weathered, is indistinctly bedded with ironstone
 132 bands, and is moderately strong to strong. However, its joint pattern shows a greater
 133 variance in spacing. The interbedded siltstones and sandstones are comprised of
 134 gradational beds of silt and sand, which can be up to 3 m in thickness, and display a widely
 135 spaced (~2 m) 'blocky' joint pattern with narrow to widely dilated joints. It is slightly
 136 weathered, is light blue-grey, and moderately strong to strong.



137
 138 Figure 2: a) Location of Staithes, North Yorkshire, UK. b) Map view of survey section and
 139 scanning location at Staithes. The location of the cliff cross-profile section presented in c)., is
 140 indicated by the cross. c) Typical cliff and lithological profile of the survey section.

141 3. Methods

142

143 3.1. Overview of approach

144 Understanding the role of rock bridges and weathering in controlling failure behaviour
145 requires complete characterisation of scar surface attributes. Both high resolution imagery
146 and 3D models of the rockfall scars derived from pre- and post-failure topography are
147 required to create and collate the scar database. From this, we undertook detailed analysis
148 of the rockfall scar texture, structure and colour to quantify the properties of broken rock
149 bridges and conversely discontinuities. This involves not only understanding the proportion
150 of each element within an individual failure surface, but also their distribution, orientation and
151 location with respect to the overall rockfall scar. Given the near-vertical cliff face and the
152 typical nature of rockfall on these cliffs (see: Rosser et al., 2013), we assume that blocks
153 delimited by pre-existing discontinuities alone must fall instantly in response to rock bridge
154 failure in an adjacent supporting block and so are indistinguishable from rockfall controlled
155 by rock bridges.

156 Firstly, we define the areal proportion of rock bridges ($\%rb$) and weathered surfaces ($\%w$)
157 within each individual rockfall scar as a percentage of the total scar surface area, and
158 proportion of weathered rock bridges ($\%wrb$) as a percentage of individual rock bridge area.
159 Respectively, these characteristics control slope stability (Jennings, 1970), indicate the
160 exposure to environmental processes (Viles, 2013), and places limits on the temporal order
161 of failure (Stock et al., 2011). Secondly, we constrain if fracturing through rock bridges is
162 either uniformly distributed across the rockfall scar, or is more locally concentrated. The
163 distribution of rock bridges determines the location, direction and magnitude of stress
164 concentration at each attachment point that supported the rockfall prior to release. Thirdly,
165 we determine the locations of rock bridges with respect to the critical slip path, which
166 influences the stress required for failure along this orientation (Tuckey and Stead, 2016).
167 Fourthly, we analyse the location of a rock bridge within a rockfall scar relative to its centre

168 of mass, which represents the location about which forces act and rotation occurs (Hibbeler,
169 2010). This places controls on failure mode, with simple moments indicating if failure was
170 most likely in tension or shear (Bonilla-Sierra et al., 2015; Stock et al., 2011).

171

172 3.2. Rockfall inventory & descriptors

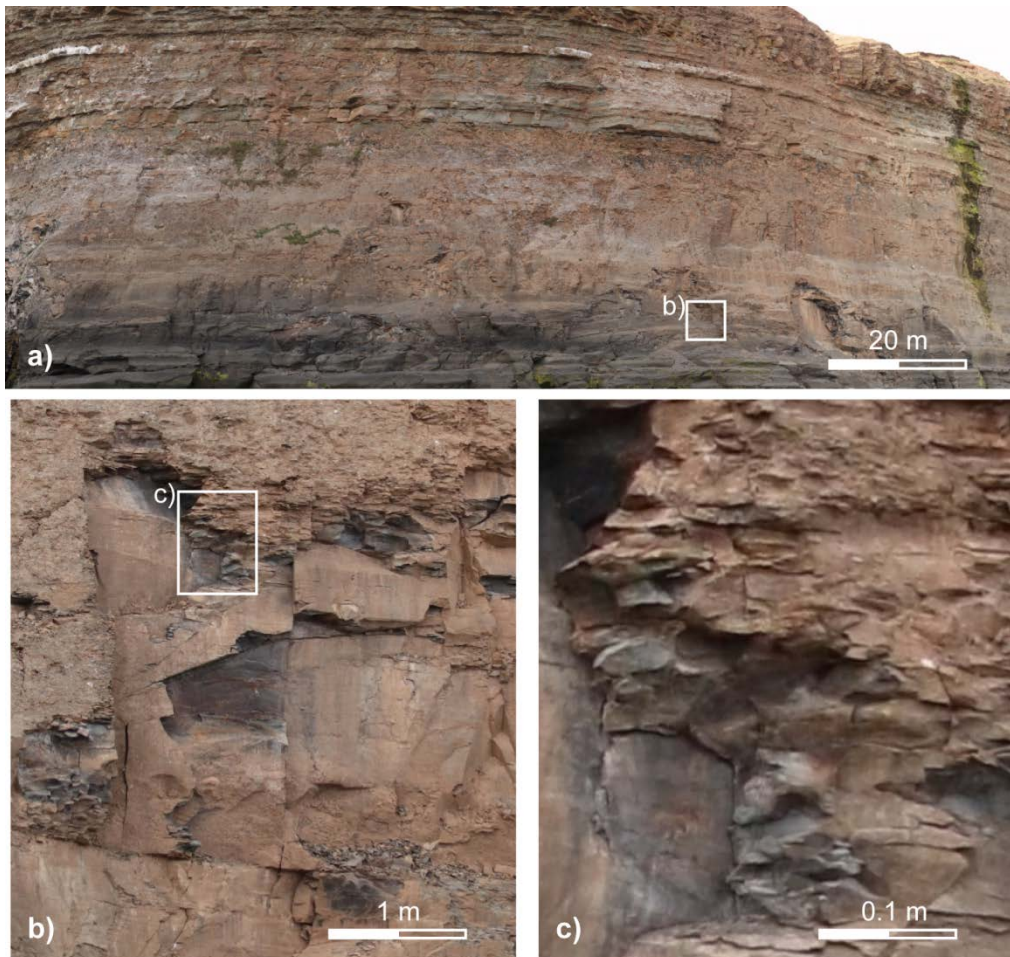
173 We collected repeat terrestrial laser scanning (TLS) surveys of a 200 m section of coast on
174 an approximately monthly basis over a 15 month period (June 2015 to September 2016)
175 (Figure 2). A Riegl VZ -1000 laser scanner was consistently positioned ~100 m from the cliff
176 toe to collect 3D point clouds with spacing of 0.01 m to 0.02 m. From this, we undertook
177 2.5D change detection of the sequential cliff surfaces using the approach detailed in Rosser
178 et al. (2005), which assumes that the cliff face can be approximated to a 2D planar surface.
179 Triangular irregular network (TIN) models were created of the pre- and post-failure
180 topography and combined to form a 3D rockfall model, from which we calculated centre of
181 the mass, volume and dimensions, assuming a uniform rock density.

182 We captured high resolution photography to provide information on surface texture,
183 discoloration due to weathering and context for interpreting the 3D scan data. We collated
184 gigapixel panoramic images of the cliff face on an approximately monthly basis over 13
185 months (August 2015 to September 2016) from the same foreshore position as the TLS
186 (Figure 2). We used a 50 MP Canon EOS 5DS R camera with a 300 mm telephoto lens, in
187 conjunction with a Gigapan Epic Pro mount. The individual photos were stitched into one
188 panoramic image (8,688 by 5,792 pixels), achieving an on-cliff pixel resolution of 0.001 m to
189 0.002 m (Figure 3). We manually adjusted aperture, shutter speed and ISO depending on
190 conditions to capture sharp, high-quality images.

191 Each panoramic image was overlaid on the DEM collected in the same month. We geo-
192 referenced the image using a spline transformation with at least 200 control points. Rockfall
193 scars were extracted from the Gigapan images using the rockfall locations extent from the

194 change measured using the TLS data comparison. Rockfall scar images that had undergone
195 distortion or warping of pixels during geo-referencing were manually deleted from the
196 database.

197



198

199 Figure 3: a) Panoramic gigapixel image of the monitored cliff section. b) Close-up of a
200 rockfall scar. c) Close-up of a freshly broken rock bridge.

201

202 3.3 Data Processing

203 Over the survey period we identified a total of 657 rockfall scars with $> 0.1 \text{ m}^2$ surface area.
204 We consider it unlikely that failures smaller than 0.1 m^2 are controlled to the same degree by
205 the interaction of discontinuity release surfaces and rock bridges due to large discontinuity

206 spacing (> 2 m) and the relatively high strength of the cliff rock as compared to small rockfall
207 volume (mass), and so these were not included in the analysis.

208 We automated the classification of rockfall scar features to avoid the subjectivity associated
209 with manual classification. This automated process involved a routine to classify areas of
210 fracture through rock bridges within the scar surface imagery. Inspection of the imagery
211 revealed that broken rock bridges in rockfall scars on these cliffs are characterised by rough
212 surfaces with micro-topography comprised of small (cm – scale) planar segments separated
213 by small (10^{-1} - 10^1 cm) linear edges, as compared to the smooth and planar pre-existing
214 discontinuity surfaces. High numbers of contiguous small segments and edges represent the
215 remnants of failed rock bridges in the scar surface. We also undertook automated colour
216 classification to identify discoloured surfaces indicative of weathering.

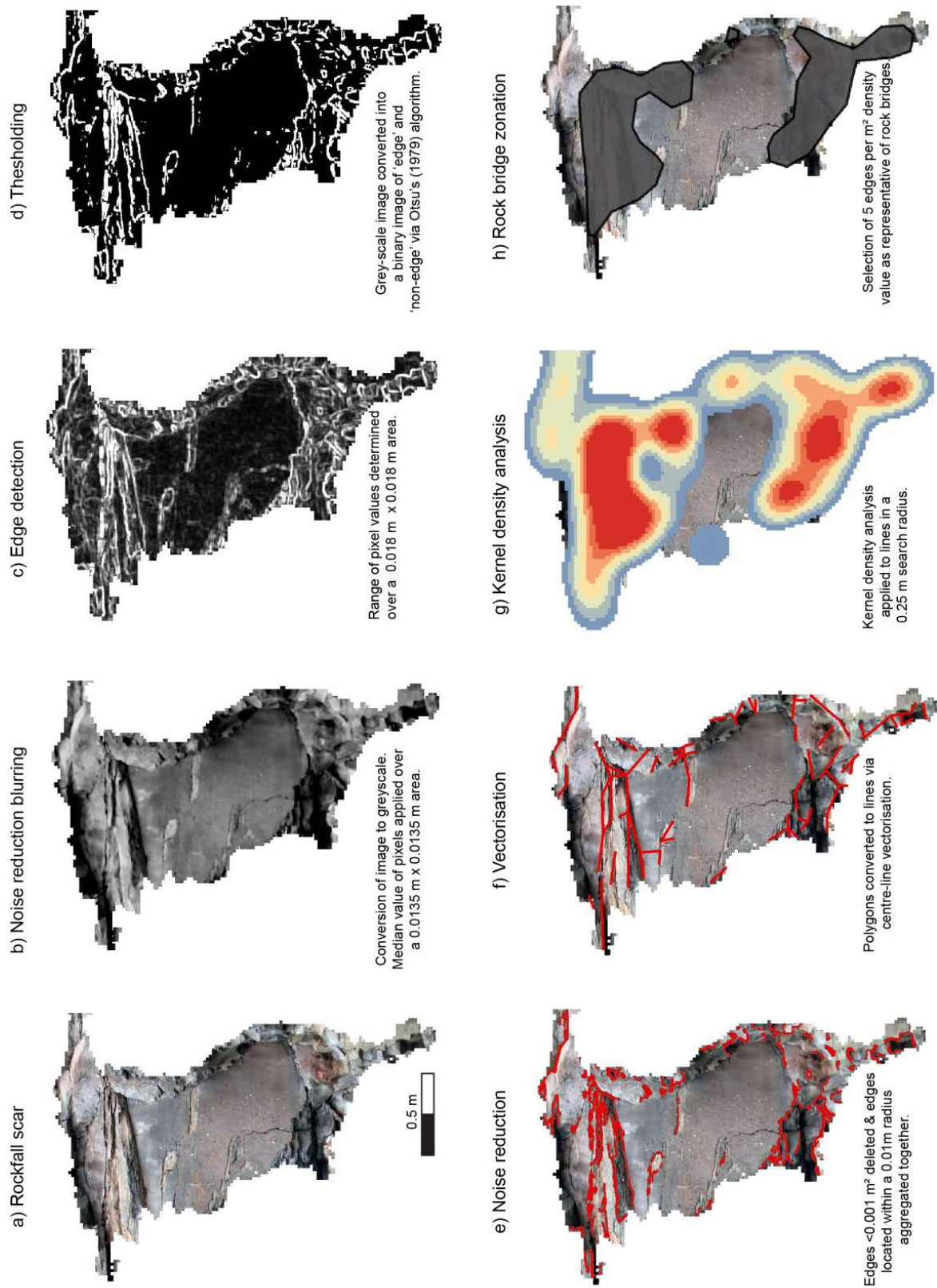
217

218 3.3.1 Edge Detection

219 To discretize the scar surface into zones of broken rock bridges and pre-existing
220 discontinuities, we developed a method to delimit areas of similar texture within the scar. We
221 employed an automated image classification technique, based upon the RGB values in the
222 high-resolution optical imagery, adapting an approach used for petrographic grain boundary
223 detection, developed by Li et al. (2008). This involves four stages outlined in Figure 4,
224 namely: edge detection, noise reduction, vectorisation and density classification. Edges were
225 detected by the contrast of light to dark tones in pixel values, indicative of shadowing created
226 by rough surfaces (Figure 4a). To enhance contrast, images were converted to grey-scale
227 and smoothed by obtaining and applying a median pixel value over a specified area to
228 reduce small scale noise (Figure 4b). As fractures are likely to have linear features and be
229 continuous within patches, pixel contrasts less than the smoothing area were considered
230 noise. The range in pixel values was calculated over a kernel size of 12 by 12 pixels or 0.018
231 m by 0.018 m, which retained resolution but remained insensitive to gradual shifts in tone

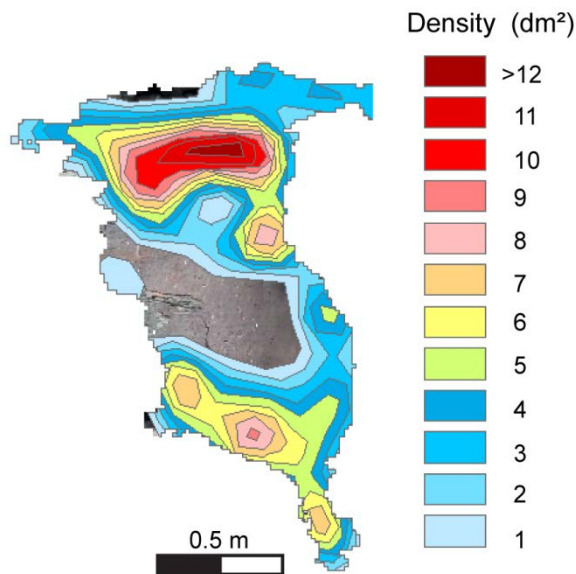
232 and/or colour due to natural lithological or weathering variations (Figure 4c). This kernel
233 highlighted only abrupt changes in pixel values, and as such identified those areas more
234 related to fracturing of intact rock. As an individual rockfall scar assessment of relative pixel
235 value range, this approach is insensitive to larger scale (e.g. month to month) variations in
236 ambient colour, and lighting. The pixel value range was converted into a binary using Otsu's
237 (1979) thresholding algorithm, allowing classification of the scar surface into zones of 'non-
238 edges' and 'edges' (Figure 4d). As this was a relative threshold value set via cluster analysis
239 of grey-scale pixel histogram rather than a pre-determined absolute value – it allowed areas
240 of relatively higher pixel contrast to be separated from areas of relatively lower pixel contrast
241 for each rockfall scar. As a second stage of noise reduction, fracture zones < 0.002 m in
242 length were omitted and those with tips within a 0.01 m area were conjugated to form a
243 continuous single 2D zone feature (Figure 4e). Zones of fracture edges were converted into
244 polylines using a centre-line vectorisation, whereby proximal collinear edges within 0.0225 m
245 were merged (Figure 4f). The line features allowed densities of fractures to be obtained
246 using a kernel with radius of 0.25 m (Silverman, 1986), which retained detail whilst
247 simplifying small-scale noise (Figure 4g). This produced coherent zones, which described
248 low to high edge densities across the rockfall scar surface (Figure 5). Areas of higher density
249 indicated fracturing through a broken rock bridge (Figure 4h), verified by visual comparison
250 of a subsample of the classified inventory.

251



252

253 Figure 4: Detailed stages of edge detection from the original image (a), through initial noise
 254 reduction (b), to edge detection algorithms(c-d), further noise reduction (e), and density
 255 analysis of edges (f-h).



256

257 Figure 5: Density classes derived from kernel density analysis of edges within rockfall scars.

258 Density increases from 1 edge per m^2 to ≥ 12 edges per m^2 within this rockfall, though

259 densities >15 edges per m^2 occur within the database. The incremental density value is

260 simplified as dm^2 .

261

262 3.3.2 Rock bridge determination

263 Based upon the density of features derived using the image classification, a threshold that

264 identifies a 'rock bridge' from other areas is needed. To determine the edge density range

265 over which features are classified as rock bridges we analysed a subset of the rockfall

266 database, which consisted of a random sample of 163 rockfall scars $> 0.1 m^2$ recorded

267 between the two monitoring intervals of 25/11/2015 and 26/01/2016,. This sub sample

268 contained a wide range of rockfall sizes and respective lithologies. Individual rock bridge

269 areas were derived from incrementally increasing density values between 1 - 15 edges per

270 m^2 (dm^2). Mean, median, interquartile range and the number of observations of individual

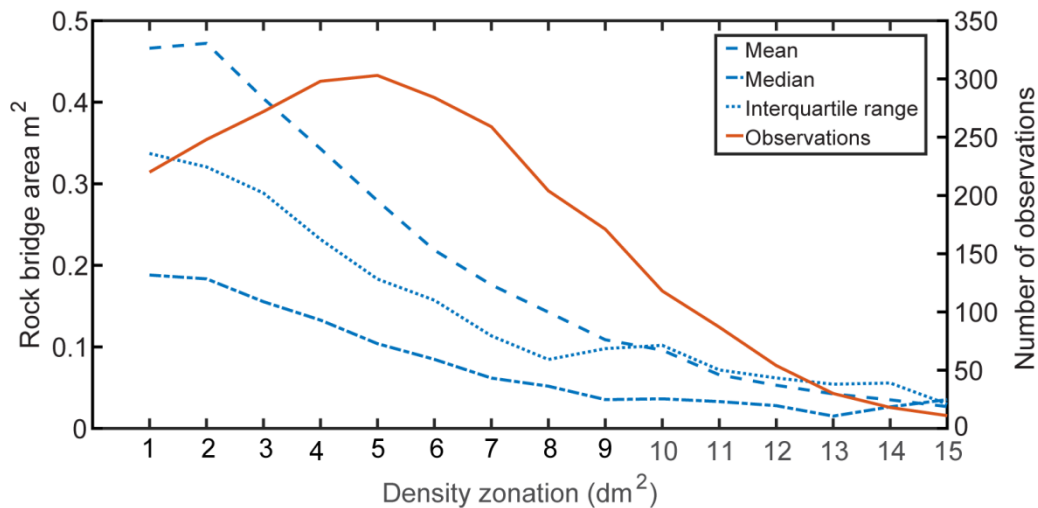
271 rock bridges (*rb_count*) for each dm^2 value were determined to evaluate the success of the

272 classification (Figure 6). The *rb_count* within a scar peaks at density values of five dm^2

273 before decreasing. At lower dm^2 rock bridges are conjoined, resulting in a lower number of
274 observations, before features become separated into several individual rock bridges when
275 using higher dm^2 (Figure 5). Above five dm^2 the numbers of observations decreases as
276 some areas no longer contain enough features to be classified as a rock bridge by the kernel
277 density analysis.

278 The mean, median and interquartile range of individual rock bridge areas decreases with
279 increasing dm^2 . On the basis of this, and in consideration with the peak rb_count , we
280 selected a density of five dm^2 for classification. Visual assessments of (>50) rockfalls scars
281 confirmed that this was a 'best-fit' for areas of dense fracturing. Additionally, we calibrated
282 this method with manual mapping of a subsample of 15 rockfall scars, which derived
283 descriptive statistics comparable to and within the margin of error of each (Table 1). Visual
284 comparison reveals that the relative location and proportion of rock bridges predicted by both
285 methods are comparable (de Vilder et al., 2017).

286



287

288 Figure 6: Descriptive values of rock bridge area recorded from different density values.
289 These densities are determined from kernel density analysis of edges recorded within
290 rockfall scars. They increase from 1 dm^2 to $\geq 15 dm^2$.

291 Table 1: Descriptive statistical comparison between automatic and manual classification of
 292 the rock bridge scar surface area.

	Mean (m ²)	Std.dev. (m ²)	Median (m ²)	Margin of error (99% confidence)*	Count
Automatic Classification	0.318	0.499	0.102	0.100	74
Manual Classification	0.191	0.283	0.100	0.157	64

293 *Due to differences in sample size a *z* (99%) and *t* (99%) confidence interval were used for
 294 the automatic (*n* >30) and manual methods (*n* <30) respectively.

295

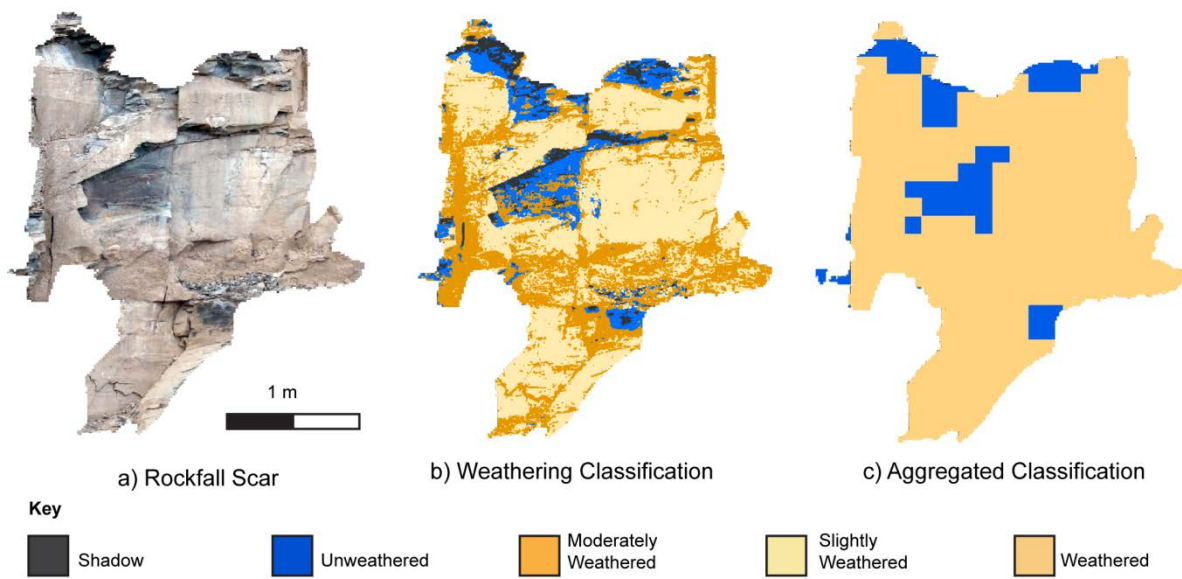
296 3.3.3 Weathering surface classification

297 We classified rockfall scars into categories to constrain the role of weathering-controlled
 298 strength degradation along discontinuities, and within rock bridge fracture (Viles, 2013).
 299 Classification was based on RGB pixel values to represent the intensity of rock weathering
 300 relative to virgin rock (Figure 7a). We manually chose characteristic RGB histogram ranges,
 301 consisting of 25 RGB samples selected to cover a wide range of different surfaces and
 302 lithologies exposed upon the cliff. These 25 samples were further classified into five
 303 categories determined via histogram evaluation and visual assessment as: unweathered,
 304 shadow, biologically weathered, slightly weathered/till covered and moderately weathered.
 305 The glacial till that caps the cliff (Figure 2) and drape debris over the cliff face making the
 306 distinction between the till cover and slightly weathered surfaces at times ambiguous.
 307 Biologically weathered surfaces contain a coating of green algae, and are often present on
 308 rockfall scars within the tidal inundation zone at the base of the cliff. To characterise the
 309 broader pattern of weathering within rockfall scars, we selected the dominant weathering
 310 types (Figure 7c). As part of this broad assessment, moderately weathered, slightly

311 weathered/till covering and biologically weathered surfaces were combined and simplified to
312 create a single weathered category.

313 We calibrated this automatic method with a manually mapped database. Comparison of
314 descriptive statistics for 15 rockfall scars (Table 2), reveal that the mean and median values
315 are comparable and within the calculated margin of error. Visual assessment of automated
316 results is comparable to the hand mapped interpretations (de Vilder et al., 2017)

317



318

319 Figure 7: Automated weathering surface classification of rockfall scar surface (a) into a
320 detailed 5 category classification of individual pixels (b) and a broader classification of 3
321 categories based on a 100 by 100 pixel area (c). Categories are outlined in the key.

322

323

324

325

326 Table 2. Descriptive statistical comparison between automatic and manual classification of
 327 the weathered scar surface area.

	Mean (m ²)	Std.dev. (m ²)	Median (m ²)	Margin of error (99% confidence)*	Count
Automatic Classification	0.264	1.044	0.025	0.212	148
Manual Classification	0.237	0.351	0.089	0.194	82

328 * Due to differences in sample size a *z* (99%) and *t* (99%) confidence interval were used for
 329 the automatic (*n* > 30) and manual methods (*n* <30) respectively.

330

331 4. Results and Interpretation

332

333 4.1 Rockfall characteristics

334 Rockfall scars in the database (*n* = 657) had a mean surface area of 0.652 m² (Table 3), with
 335 13% of rockfall scars having a surface area > 1 m². We use scar surface area as a metric for
 336 rockfall size, as it provides a consistent comparison with %*rb* and %*w*, and has positive
 337 linear relationship with measured rockfall volume (*r* =0.927, *p* = -0.033). Rockfalls are
 338 distributed from across the cliff face, with the highest concentration observed in the shale
 339 units (54% in the upper shale and 28% in the lower shale). Fewer interbedded siltstone and
 340 sandstone rockfalls are captured due to their location within the cliff face. These events
 341 were commonly discarded due to pixel distortion as a result of both the relative steep angle
 342 of data capture and nature of 'stretching' the panoramic image over the protruding
 343 sandstone and siltstone beds. .

344

345

346 Table 3: Characteristics of rockfall volume, area and simple geometric variables within the
 347 database.

	Area (m ²)	Volume (m ³)	Width (m)	Height (m)	Depth (m)
Mean	0.652	0.236	1.076	0.893	0.652
Median	0.233	0.043	0.760	0.660	0.494
Std.dev.	1.534	1.208	0.971	0.722	0.547
Min	0.100	0.010	0.260	0.083	0.175
Max	26.912	27.003	9.560	6.160	3.956
Range	26.812	26.993	9.300	6.077	3.781

348

349

350 4.2 Rockfall scar characteristics

351 4.2.1 Rock bridge and weathering proportions

352 The distribution of %rb displays a wide range in values with a skewness of 0.4, and peak in
 353 observations for < 2 %rb (Figure 8a). This includes rockfalls with no rock bridges, which
 354 account for 20% for rockfalls within the database. Such rockfall are predominately < 0.2 m²
 355 with a maximum scar surface area of 1.66 m² (Figure 9). Excluding this subset, %rb values
 356 are normally distributed with a wide range in values from 0% to 97.6%, and a mean value of
 357 31% ± 26% and a median of 29% (Figure 8a and Table. 4). Individual rockfall scars therefore
 358 display a large range in the proportion of their surface that comprises broken rock bridges.

359 To understand what drives this large range in %rb values, we assessed rockfall volume and
 360 lithological differences. Rockfall scar area showed no correlation with %rb ($r = -0.122$, $p =$
 361 0.006), with a wide scatter in %rb. Comparison of descriptive statistics between the three
 362 lithologies revealed a 10%rb difference by rock type (Table 4). The lower shale displayed the
 363 lowest %rb (26.7%) and interbedded siltstones and sandstones displayed the highest (%rb =

364 34.7%). A similar pattern is observed for the median values of %rb. Analysis of variance
365 indicates that the lower shale unit had a statistically-significant ($p = 0.01$) lower mean %rb
366 than that of the upper shale and siltstone/sandstone units. Therefore, %rb varies as a
367 function of lithology but not with increasing rockfall size. The different lithological units, and
368 their associated rock mass structure, can be considered a critical influence on the
369 prevalence of rock bridge proportion within the scars (and therefore rockfalls) that each unit
370 generates.

371 %w has a bimodal distribution whereby rockfalls are generally characterised by either <4
372 %w, or more strongly at values of >98 %w surface weathering (Figure 8b). There is a wide
373 but consistent range in values between these two end members, which generates a mean
374 value of $49.7\% \pm 34.9\%$, and a median of 48.9%. Surfaces with >98 %w correspond to the
375 peak in values for <2%rb, suggesting that rockfalls with nearly 100%w contain 0%rb.
376 However, as the peak is larger for %rb, some of these scar surfaces with no rock bridges
377 must have been partly unweathered prior to failure. This suggests that %w is not solely
378 related to discontinuity occurrence within the rockfall scar, and as such must be related to
379 weathering of already broken rock bridges. The wide range in values also indicates that
380 discontinuity connectivity within the rock mass influences the distribution of weathering
381 across the scar surface prior to failure.

382 %wrb has a similar bimodal distribution to %w with rock bridges strongly >98%wrb or <20
383 %wrb, and a wide consistent range in values (Figure 8c). %wrb has a mean value of 43.51%
384 $\pm 35.19\%$, and a median value of 35.5%. Most rock bridges however are only partly
385 weathered, with 79.95% of all rock bridges containing <50%wrb, and %wrb overall accounts
386 for 12.99% of total rock bridge area. This may be a function of the areal aggregation during
387 classification and the ambiguity of classifying till covered/slightly weathered surfaces (Figure
388 7), introducing an element of uncertainty in this result. As such, we suggest that the broad
389 pattern of these results rather than the exact %wrb value is more important. The result
390 implies that some rock bridges within the rock mass have been either partially or completely

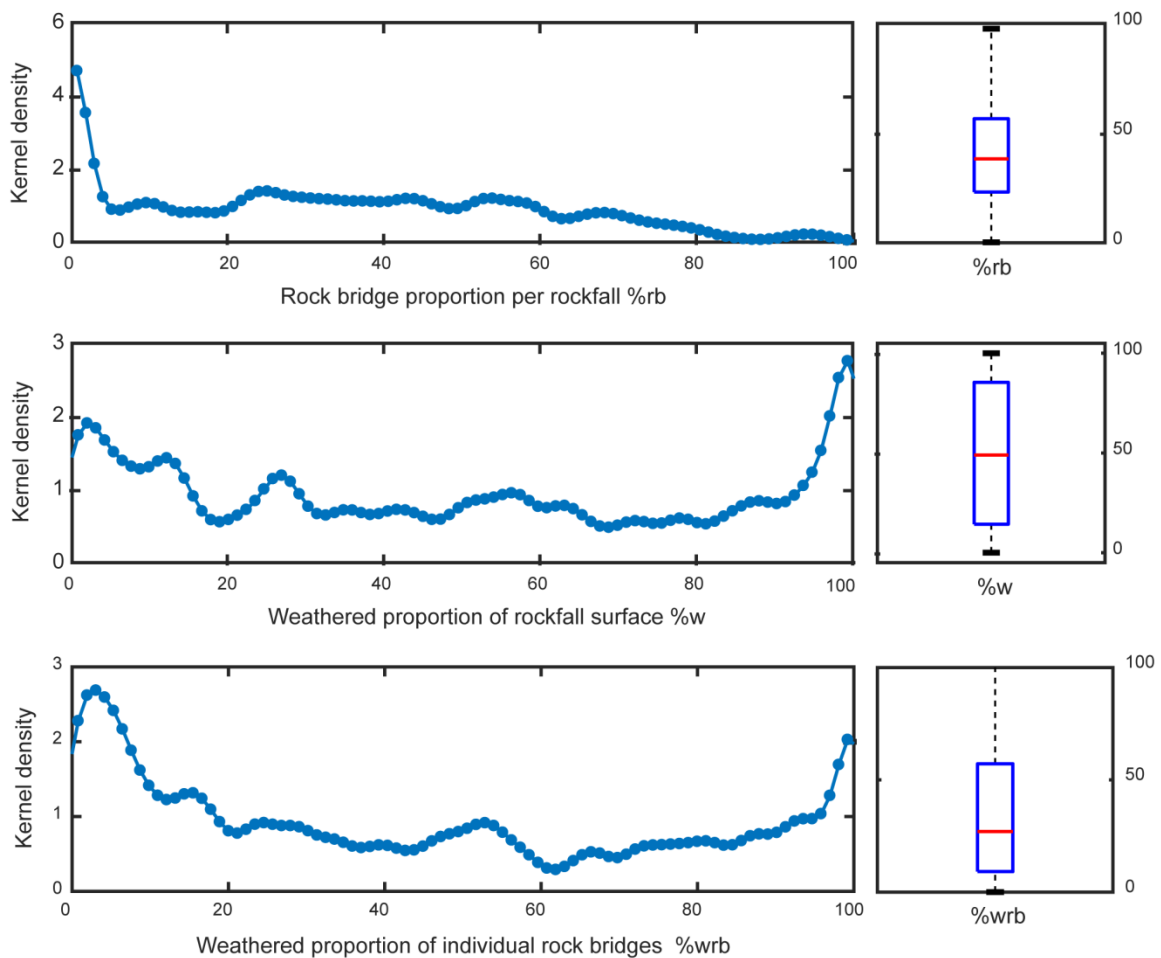
391 fractured before final failure of the rockfall, and these fractured surfaces have been exposed
 392 for a significant periods of time for surficial weathering and discolouration to take place.

393

394 Table 4: Descriptive statistics for %rb based on geology

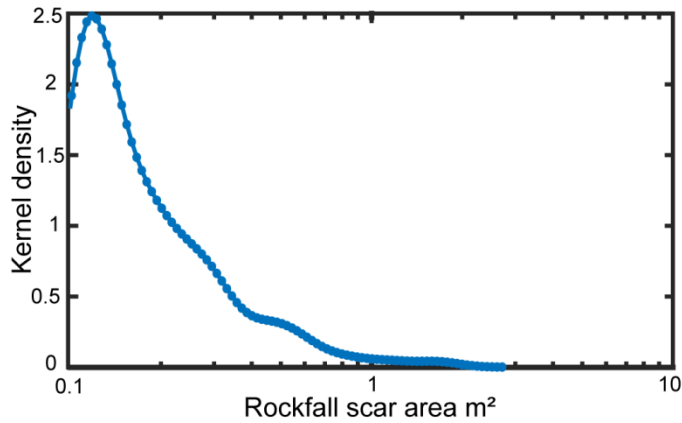
	Mean	Std.dev.	Median	Max	Min	Count
All	30.8	25.8	28.9	97.6	0	657
Lower Shale	26.2	26.7	20.3	97.6	0	184
Upper Shale	31.9	25.1	31.2	95.3	0	356
Siltstone/Sandstone	34.7	25.9	36.2	93	0	117

395



396

397 Figure 8: Histograms and box plots of a) %rb and b) %w and c) %wrb.



398

399 Figure 9: Kernel density plot of the area distribution of rockfall scars recorded with no rock
 400 bridges.

401

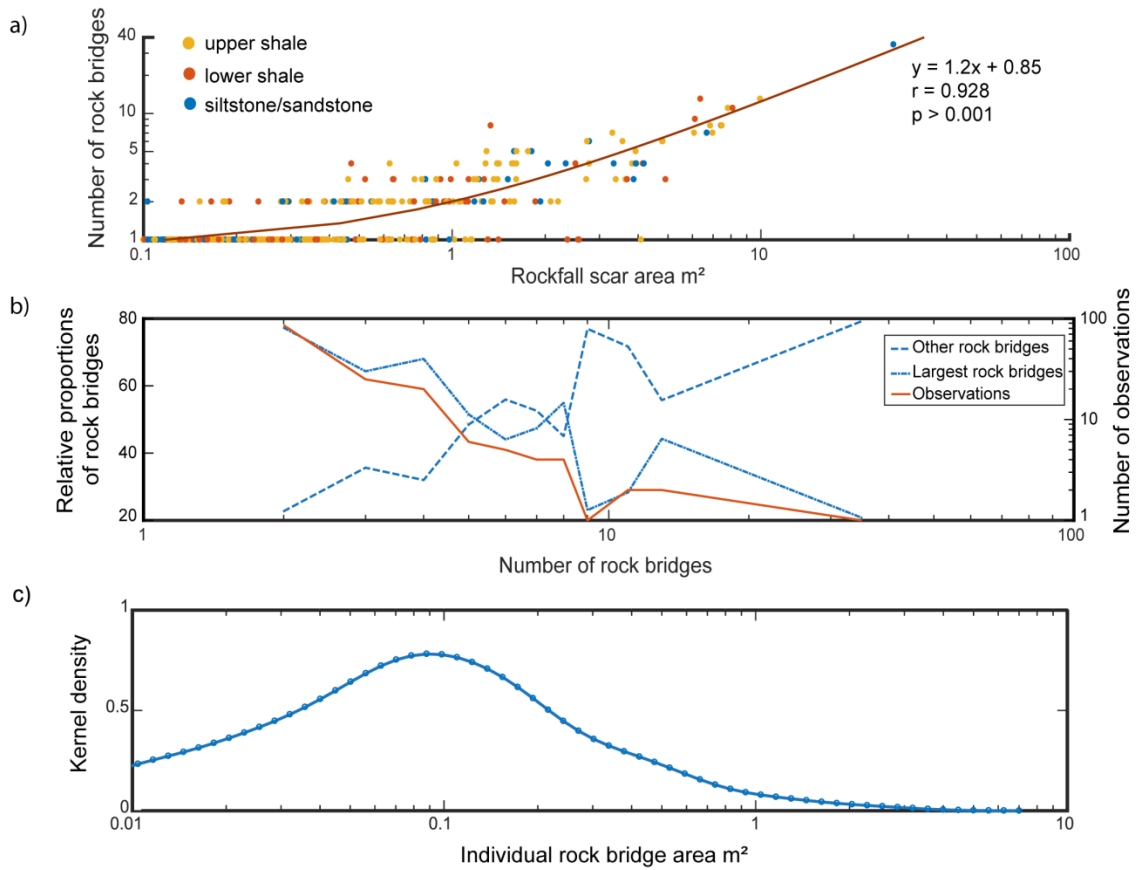
402 4.2.2. Rock bridge distribution

403 Rockfalls have a median value of one rock bridge per scar, with a mean value of 1.8 ± 2.2 .

404 The number of rock bridges per scar has a significant positive linear correlation with
 405 increasing rockfall scar area ($r = 0.928$; Figure 10a). This demonstrates that larger rockfalls
 406 contain more individual rock bridges, as opposed to larger rockfalls purely being larger
 407 versions of their smaller counterparts. Mechanically, larger rockfalls may therefore behave
 408 and fail in a manner quite different to smaller rockfall, and so may be sensitive to a different
 409 set of conditions, controls or thresholds on failure. Around 0.5 m² scar surface area, rockfalls
 410 tend to contain ≥ 2 rock bridges, with the trend indicating that rockfalls with 1 m² surface area
 411 are most likely to contain two or more rock bridges. This indicates that, in broad terms for
 412 every 0.5 - 1 m² of increasing rockfall scar surface area, there is one additional rock bridge
 413 holding the block to the rock face. Individual rock bridge area is predominantly measured to
 414 be c. 0.1 m² (Figure 10). A 0.5 m² rockfall surface area that contains a 0.1 m² rock bridge
 415 adheres to the mean %rb estimate.

416 Within each rockfall scar, we examined the areal extent of the individual rock bridge(s)
417 (Figure 10b). We compared the relative area of the largest rock bridge within the scar to all
418 the other rock bridges within the same scar. Our analysis identifies that for rockfalls with <5
419 rock bridges, one main rock bridge dominates the scar surface, with smaller peripheral
420 bridges. As the number of rock bridges increases the dominance of a single bridge
421 decreases, as the fraction of the scar rock bridge area occupied by the largest rock bridge as
422 compared to all other rock bridges reduces. This suggests that for larger rockfalls with > 5
423 rock bridges in the inventory, rock bridges tend to be of a similar surface area. Conceptually,
424 and assuming a homogenous rock mass structure, as the failure scar surface area grows it
425 incorporates more rock bridges. With increasing rockfall volume, fractured rock is distributed
426 across multiple bridges of similar size, rather than concentrated in one primary rock bridge.
427 By implication the perimeter to area ratio of rock bridges changes with rockfall volume, which
428 exposes a greater area of the supporting rock bridges to be exposed to weathering within
429 the rock mass.

430



431

432 Figure 10: a) Scatter plot displaying a positive linear trend between number of rock bridges
 433 per scar and rockfall scar area. b) Mean values of the relative proportion of the largest rock
 434 bridge within an individual scar compared with the proportion of all other rock bridges within
 435 an individual scar. For example, if a rockfall scar contains two rock bridges, the largest
 436 accounts for 80% of rock bridge area while the other accounts for only 20 %. The number of
 437 observations for the calculation of mean values is plotted on the right axis and decreases
 438 with increasing rock bridges. c) Kernel density plot of individual rock bridge area distribution,
 439 displaying that most rock bridges are 0.1 m².

440

441 4.2.3 Rock bridge orientation

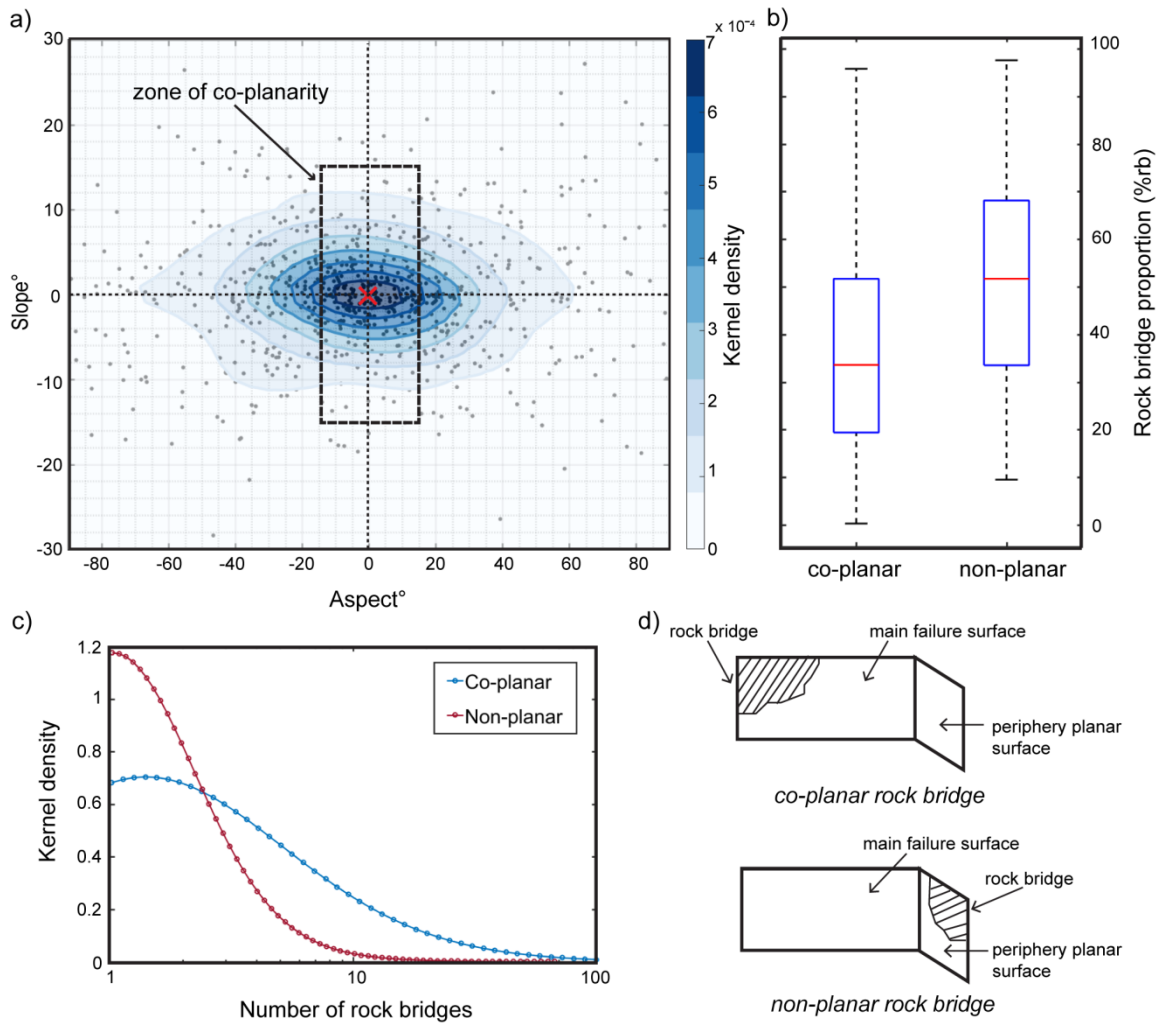
442 We assessed the orientation of rock bridges with respect to rock bridge planarity relative to
 443 the main failure surface. We compared the mean slope and aspect (derived from the cliff

444 face surface topography model) of the rock bridges with that of the overall aspect and slope
445 of the scar surface (Fig 11a). Slope and aspect are comparable to the dip and dip direction,
446 respectively, of a discontinuity given the projection of the cliff face data employed here. Scar
447 aspect was measured relative to cliff normal (Figure 2b) and as such represents deviations
448 from the cliff face aspect. From this we derived a mean aspect value of $173.7^\circ \pm 53.1^\circ$,
449 indicating that the most rockfall scars are oriented approximately parallel to the cliff face.

450 We define rock bridges as co-planar with the main failure surface, if both slope and aspect
451 are $\leq 15^\circ$ from scar surface orientation. Due to the relatively small failure size and based on
452 field observation, we assumed rockfalls scar surfaces contained one main planar failure
453 surface, and therefore co-planar rock bridges are also in-plane with this surface. We define
454 rock bridge deviations in slope and aspect of $>15^\circ$ as non-planar. Our definition of non-
455 planar bridges does not necessarily distinguish in-plane rock bridges along intersecting joints
456 from out-of-plane rock bridges located between discontinuities of differing orientations.
457 69.5% of rock bridges were defined as predominately co-planar, with 30.5% predominantly
458 non-planar. Rockfalls that contain both non-planar and co-planar rock bridges account for
459 14.8% of events in the inventory. For these rockfalls, scars are dominated by co-planar rock
460 bridges (97%), with non-planar rock bridges forming only a minor component of the total
461 scar. Therefore, nearly all rockfalls which contained both non-planar and co-planar bridges
462 were accounted for within the 69.5 % of rock bridges which are predominately co-planar.
463 This suggests that lateral release surfaces related to discontinuities striking perpendicular to
464 the cliff face contain fewer rock bridges. Assessment of mean *rb* between co-planar and
465 non-planar rock bridges reveals that non-planar rock bridges show a higher proportion
466 (51.1%*rb*) compared to co-planar (35.4%*rb*) (Figure 11b). Analysis of variance indicates that
467 this difference is statistically significant ($p > 0.001$), so although non-planar rock bridges are
468 less prevalent in our dataset, when they are recorded, their *rb* is normally higher. Analysis
469 of the distribution of co-planar versus non-planar rock bridges shows that (larger) rockfalls
470 with multiple rock bridges are less likely to contain non-planar rock bridges (Figure 11c).

471 Therefore, non-planar rock bridges are limited to smaller rockfalls, which as identified
 472 previously, tend to contain only one rock bridge. These smaller rockfalls are more likely to be
 473 associated with discontinuity surfaces, which comprise rock bridges, whereas the larger
 474 rockfalls have fractured both through and across discontinuities.

475

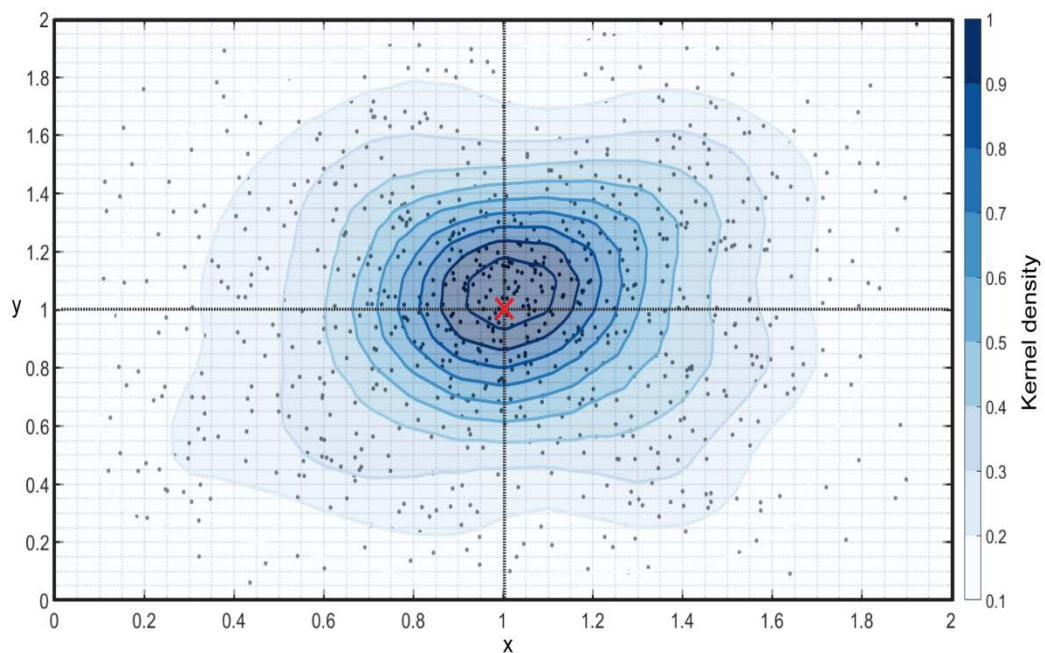


476

477 Figure 11: a) Kernel density plot displaying the difference in mean slope and mean aspect
 478 between rock bridge and the rockfall scar surface. Co-planarity defined as change in slope &
 479 aspect of < 15 °. b) Box plot displaying difference in % *rb* between co-planar and non-planar
 480 rock bridges. c) Kernel density plot of the number of rock bridges for either co-planar or non-
 481 planar rock bridges. d) Conceptual end-member examples of co-planar and non-planar rock
 482 bridges.

483 4.2.4 Rock bridge location

484 We normalise the coordinates of the position of the centre of the rock bridge relative to the
485 coordinates of the 3D centre of mass projected back onto the cliff face for each rockfall. The
486 centre of the rockfall is located at coordinates {1,1}, and rock bridge positions are displayed
487 relative to this point (Figure 12). The highest density of rock bridges is generally located just
488 above the rockfall centre of mass. Overall, more rock bridges are located above the rockfall
489 centre of mass (52.4%), as opposed to below (47.6%), although this distinction is not clear.
490 Rock bridges are however clustered around the projection of the rockfall centre of mass onto
491 the cliff, with a decreasing density in bridge position with increasing radial distance relative to
492 the scar extent. Rock bridges are broadly represented in all areas of the rockfall scar, except
493 on the very periphery. Rock bridges therefore may not define the perimeter of the rockfall,
494 but rather support a mass of which the extent is defined by the rock mass structure.



495

496 Figure 12: Kernel density plot of rock bridge centres normalised to the rockfall centre of
497 mass. The rockfall centre is located at the x of 1, 1- with y values < 1 located below the
498 rockfall centre and y values > 1 located above the rockfall centre.

499 5. Discussion

500 5.1 Rock bridge role in failure

501 Our results demonstrate that a wide range of *%rb* is possible within failures from the same
502 rock type and structure. This holds across a range of rockfall sizes, but varies with source
503 rock lithology. The mean *%rb* value of 31% \pm 26% is higher than previously reported for other
504 rockfall scar analysis case studies, which invariably focus on larger volume events, often in
505 more competent or massively jointed rock. Previous studies, comprising of individually
506 mapped rockfall scars, displayed a range of 0.2% to 26% (Frayssines and Hantz, 2006; Lévy
507 et al., 2010; Paronuzzi et al., 2016; Paronuzzi and Sera, 2009; Stock et al., 2012, 2011).
508 Estimates obtained from discontinuity persistence mapping and back analysis modelling
509 display a larger range of 1% to 45% (Elmo et al., 2011; Gischig et al., 2011; Grøneng et al.,
510 2009; Karami et al., 2007; Matasci et al., 2015; Sturzenegger and Stead, 2012; Tuckey and
511 Stead, 2016). All of these estimates, including our dataset, display a six order of magnitude
512 range in rockfall size (from 0.01 m³ to 10,000 m³) and consider various rock types.

513 We suggest that the large recorded variance in *%rb*, which we report here, is due to the
514 spatial distribution of rock bridges within the slope, as determined by the persistence and
515 spacing of discontinuities within the rock mass (Tuckey and Stead, 2016). To account for this
516 variance, robust sensitivity analysis within modelling to determine failure susceptibility is
517 needed. Through analysis of rockfall scars from the three rock types considered here, it is
518 evident that lithology is an important control on rock mass strength in defining the nature of
519 rock bridges, and even subtle changes in rock mass structure between the three lithological
520 units results in significant *%rb* differences. This indicates that not only the wider geology, but
521 also the local scale lithology changes control rock mass characteristics that are important
522 controls in releasing blocks as rockfall. Joint density, a proxy for joint spacing, varies with
523 bed thickness (e.g. Huang and Angelier, 1989; Ladeira and Price, 1981; Narr and Suppe,
524 1991), indicating that within interbedded sedimentary sequences rock bridge characteristics
525 will vary as function of mechanical stratigraphy.

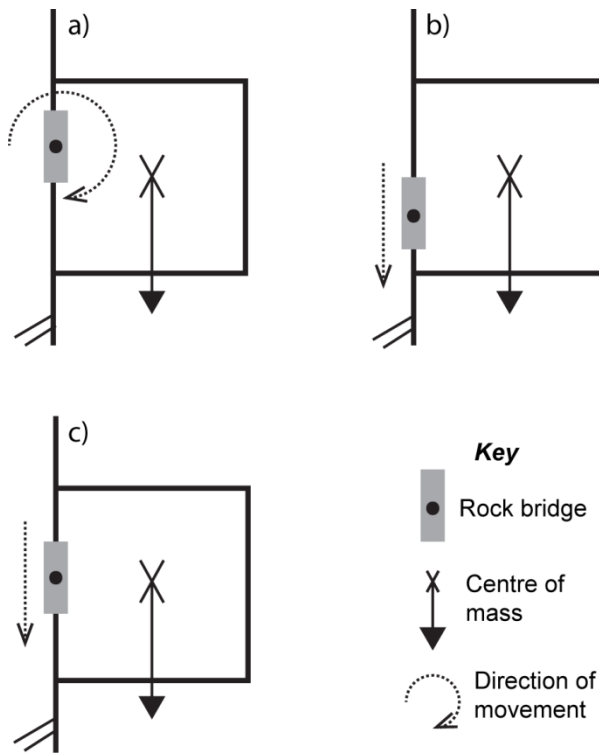
526 The distribution of these rock bridges influences the stress within the incipient failing mass,
527 determining its eventual failure mode (Bonilla-Sierra et al., 2015; Stock et al., 2011). Our
528 dataset demonstrates that most rockfalls in our inventory will contain a singular rock bridge,
529 which may be located throughout the scar, except on its periphery, with an approximately
530 equal location probability above or below the rockfall centre of mass. Bonilla-Sierra et al.,
531 (2015) modelled rock bridge location in relation to a translational failure. Higher
532 concentrations of tensile cracking were associated with rock bridges located at the top of the
533 failure surface, a steeper slope angle and a lower centre of mass. When the rock bridge is
534 located above the centre of mass, and assuming simplified geometry, the force acting on the
535 failure mass generates a bending moment that results in greater tensile cracking and
536 associated rotation (Hibbeler, 2010). Conversely, shear cracking was associated with a more
537 shallow failure surface and rock bridges located in the centre or lower parts of failure
538 (Bonilla-Sierra et al., 2015). Using a similar simplification, we suggest that rockfalls with rock
539 bridges located above the centre of mass likely fail predominantly in tension, while rockfalls
540 with rock bridges in line with or below centre of mass are likely to predominantly fail in shear
541 (Figure 13). The degree of deviation of rock bridge location from the rockfall centre needed
542 to generate sufficient bending moment and associated tensile failure is unknown. Further
543 modelling would reveal if even slight deviations in rock bridge location results in an
544 imbalance of forces, affecting those acting on a failing block and resulting in a change to the
545 dominant failure mode.

546 Additionally, rock bridges that are non-planar to the main failure surface or located to the
547 side of the centre of mass introduce an element of twisting or torsion into the mechanical
548 analysis, which is rarely considered within the 2-dimensional analysis of slope failure
549 mechanics (e.g. Wyllie and Mah, 2004), but is standard practice for structural engineering
550 (e.g. Hibbeler, 2010). These require a fully 3D approach to account for dilation and rotation
551 of blocks within the rock mass. Analysis of the stresses experienced by the rock bridges will
552 determine which strength characteristics, such as tensile or shear, are most important for

553 stability. We show here that with increasing rockfall size, more rock bridges are likely to be
554 incorporated into the eventual failure surface. This increases the complexity of the forces
555 acting on the incipient failure mass due to their multiple attachment points to the slope. This
556 also highlights the potential for the sequential failure of one rock bridge at a time, and the
557 subsequent transfer of and changes in the nature of stress on remaining intact bridges.

558 Our results show that smaller rockfalls containing <5 rock bridges are commonly dominated
559 by one large main rock bridge, which dictates the potential for failure and release. The
560 mechanical and compositional characteristics of this main bridge will determine its strength,
561 and the magnitude and trajectory of stress required for failure to occur. Within a
562 heterogeneous (sedimentary) lithology, small scale (10^{-3} m to 10^0 m) intrinsic flaws such as,
563 micro-cracks, grain boundaries and sedimentary structures, such as ripples or concretions
564 may predispose the rock bridge to failure by forming initiation points for micro- and macro-
565 crack propagation (Kranz, 1983; McConaughy and Engelder, 2001; Pollard and Aydin,
566 1988). As such, the temporal behaviour of these smaller rockfalls may be difficult to predict.

567 As a failure develops, it remains unclear how the failure responds to, accommodates and
568 incorporates smaller peripheral rock bridges, or includes the partial failure of larger rock
569 bridge located on the edge of failure scar. In the case of a partial failure of a larger rock
570 bridge, questions concerning controls on termination of fracture within that rock bridge and
571 the impact on the dimensions of the failure mass are raised. This point of termination may be
572 determined by intersecting cliff perpendicular discontinuities or non-persistent bedding,
573 whereby fracture propagation deflects and stops at these boundaries due to changes in the
574 near-field stresses experienced by the propagating crack tip, influenced by changes in
575 lithological composition and mechanical interactions with discontinuities (Pollard and Aydin,
576 1988; Scavia, 1990). Therefore, discontinuity spacing may control rockfall geometry and the
577 amount of partial and complete fracturing required through rock bridges contained within the
578 incipient failure mass.



579

580 Figure 13: Conceptual model of rock bridge attachment points and potential failure
 581 directions. a) Rock bridges located above centre of mass may result in outward rotation of
 582 the incipient rockfall block and associated tensile failure. b) & c) Rock bridges located below
 583 centre of mass may fail in shear due to downward forces acting on the rock bridges.

584

585 5.1 Implications for progressive failure

586 For larger rockfalls, fracturing through each of the multiple rock bridges is required. The
 587 order through time in which rock bridges fracture remains poorly constrained, but is likely to
 588 be complex. This order must have important implications for progressive failure and stress
 589 redistribution within the incipient scar (Eberhardt et al., 2004; Kemeny, 2003; Stead et al.,
 590 2006). For instance, the fracture of minor rock bridges may result in significant enough
 591 changes to stress distribution to create instability, or it may only be the fracture of larger
 592 bridges that are the catalyst for acceleration towards final failure and block release.
 593 Fracturing may represent or may drive pre-failure deformation (e.g. Rosser et al, 2007;

594 Kromer et al., 2015) whereby observed surface deformation may be a manifestation of
595 fracturing of rock bridges within the rock mass. Our analysis of %*wrb* distribution has
596 indicated that substantial weathering of fractured rock bridges can occur before final failure,
597 suggesting that pre-failure deformation may not always result in a sudden acceleration
598 towards failure and may evolve over a period sufficiently long enough for weathering to take
599 hold. In these circumstances the redistribution of stress may result in a new prolonged
600 (quasi-)equilibrium state (Leroueil, 2001). Modelling of progressive failure may help
601 understand this temporal pattern by accounting for the distribution of fracturing and stress
602 between these multiple rock bridges (Stead et al., 2006).

603 Rockfall failure is commonly poorly correlated with environmental conditions and can occur
604 entirely independently of environmental triggers (Lim et al., 2010; Rosser et al., 2007).
605 However, smaller rockfalls (< 0.1 m³) can be more successfully correlated to, for example,
606 mean air temperature and wind velocity (Lim et al., 2010). These correlations may exist for
607 small rockfalls that display no rock bridges, and as such require no fracturing through intact
608 rock to instigate release. For rockfalls with rock bridges, some form of rock strength
609 weakening is needed for failure to occur at low magnitude environmental stress triggers that
610 are otherwise insufficient to fracture intact rock (Gunzburger et al., 2005). This weakening is
611 likely to be driven by processes such as weathering or stress redistribution as described
612 here (Collins and Stock, 2016; Gunzburger et al., 2005; Viles, 2013). These processes can
613 create stress fluctuations within the slope that drive the development and coalescence of
614 micro-cracks, eventually reducing the strength of rock to the point of failure (Attewell and
615 Farmer, 1973; Cruden, 1974; Stock et al., 2012).

616 Our analysis shows that the rockfalls considered here display a wide range of exposure to
617 weathering prior to failure, as represented by the variation in %*w* and %*wrb*. However, not all
618 discontinuity surfaces may be weathered, with the prevalence determined by the connectivity
619 of the discontinuity sets and the intensity and efficacy of environmental conditions acting on
620 and within the slope. The relationship between this exposure and connectivity influences

621 weakening within the slope (Gischig et al., 2011; Viles, 2013). Weathering at the interface
622 between a rock bridge and a discontinuity, known as the crack tip, where stress is
623 concentrated, is an important control on weakening and fracture propagation (Collins and
624 Stock, 2016). The rock bridge perimeter to rock bridge area ratio must to some extent dictate
625 this rate of weakening of rock bridges. For example, two slopes with the same overall rock
626 bridge proportion may weaken at different rates depending on rock bridge size, shape, area
627 and distribution. A slope that contains smaller but more abundant rock bridges may weaken
628 at a faster rate due to high perimeter to area ratio.

629 As attachment points to the slope, rock bridges represent zones of stress concentration.
630 Recent research has shown a complex relationship between weathering and stress prior to
631 failure, which suggests that stress concentrations may either enhance or dampen the
632 efficiency of weathering events (Brain et al., 2014; Bruthans et al., 2014). Understanding the
633 stress regime that rock bridges experience can determine their temporal and spatial
634 response to weakening (Kemeny, 2003). Micro-cracks may be preferentially oriented with
635 respect to the applied stress (Brain et al., 2014), impacting overall strength. For example
636 mode 1 cracking will reduce tensile intact rock strength. The models presented by Scavia
637 and Castelli (1996) indicate that fracture propagation is dependent on rock bridge size, with
638 larger rock bridges requiring tensile σ_3 conditions - the minimum principal stress, for fracture
639 to occur. Defining rock bridge proportion and distribution, along with failure mode, is critical
640 for assessing the failure stress regime. The exact nature of feedbacks between weakening,
641 the stress regime and individual failures, and how these interactions drive the propagation of
642 further failure requires detailed quantification. These interactions affect the timing of rockfall
643 failure, which holds implications for the frequency and magnitude of rockfall activity, a critical
644 input of hazard assessments (Fell et al., 2008) and slope erosion rate calculations (Barlow et
645 al., 2012; Dussauge et al., 2003; Malamud et al., 2004).

646

647 5.2 Influence on rock mass strength

648 We observe that while most rock bridges are co-planar to the main failure surface, ~30% are
649 not. These non-planar rock bridges may represent fracturing through intact rock along
650 discontinuity sets, or the partial fracturing of peripheral rock bridges co-planar to the failure
651 surface. Non-planar rock bridges are largely absent from larger rockfalls, suggesting that
652 they are representative of partial fracturing through peripheral rock bridges, or that they have
653 been subsumed into the failed mass and so are not visible within our analysis. This indicates
654 that most rock bridges are located co-planar to the main failure surface, which in this
655 instance is cliff parallel. The prevalence of rock bridges along cliff parallel discontinuities may
656 be related to the conditions of joint formation. These cliff-parallel joints may be formed in
657 response to local scale topographic stress and slope curvature (Gerber and Schiedegger,
658 1969; Martel, 2017). It is unlikely that these discontinuities represent large scale sheeting
659 joints, like those observed in the granitic rocks of Yosemite valley, due to the lower
660 magnitude of overburden stress and weaker lithologic characteristics of the rocks considered
661 here (Martel, 2017). We however assume that smaller scale topographic stresses may
662 generate smaller scale fracturing comparable in form if not scale.

663 These localised topographic stresses may result in an intermittent smaller-scale joint
664 propagation. Additionally, as joint density increases within a rock mass, the interactions
665 between the individual joints inhibit each other's expansion (Pollard and Aydin, 1988), by
666 changing the stress intensity factor of the propagating crack tip of a joint (Scavia, 1990). This
667 results in less persistent but higher density jointing with a greater prevalence of rock bridges,
668 distributed in distinct zones within the slope. In contrast, intersecting joints, which may have
669 been formed by larger regional scale stresses associated with tectonics and uplift, may be
670 more persistent separated by larger rock bridges (Brideau et al., 2009; Tuckey and Stead,
671 2016). Our analysis reveals that non-planar bridges account for a higher proportion of scar
672 surface area. Therefore, the spatial prevalence and pattern of rock bridges within a slope is
673 related to its rock mass strength characteristics as determined by joint type. The propagation

674 and persistence of joints in turn is influenced by lithology (Pollard and Aydin, 1988). Defining
675 the conditions of joint formation and their resulting characteristics will enhance our
676 understanding of rock mass strength (Moore et al., 2009). Consequently, this has
677 implications for slope evolution, with numerous studies outlining the influence of rock mass
678 strength on differential slope forms (Augustinus, 1992; Moore et al., 2009; Selby, 1982).
679 Understanding the intrinsic properties of rock mass strength, as represented by rock bridges,
680 discontinuities and weathering, will better inform the parameters of larger scale landscape
681 evolution models (Moore et al., 2009).

682

683 6. Conclusions

684 We present the first large scale database of rock bridge and rockfall scar weathering
685 characteristics (0.1 m² to 27 m²). Our analysis reveals:

- 686 • Rock bridges account for 31% ±26% of failure scar surface area. The wide range in
687 %rb is related to subtle changes in lithology and rock mass structure.
- 688 • Failure mode is dependent on the imbalance of mass created by the deviation
689 between the rockfall centre and rock bridge attachment point. This point may be
690 subjected to tensile, shear and torsional stresses, which influences the parameter of
691 strength critical for stability. 3D modelling is required to provide a comprehensive
692 slope stability analysis.
- 693 • The number of rock bridges within a scar, and associated failure complexity, increase
694 linearly with rockfall size. The majority of rockfalls are dominated by one main rock
695 bridge, which is critical for maintaining stability. For larger rockfalls to fail, progressive
696 failure and fracturing is likely required through multiple rock bridges. Through time
697 the stress applied to each rock bridge may change as it tends towards being the next
698 in sequence to fail.
- 699 • Rock bridges must have been weakened prior to failure, with the rock bridge

700 perimeter to area ratio determining weathering exposure at the discontinuity/rock
701 bridge boundary. Not only is rock bridge proportion a control on stability, but other
702 rock bridge attributes are important to provide a full explanation of the spatial and
703 temporal occurrence of failure.

- 704 • Rock bridges provide controls on the mode, spatial pattern, and temporal behaviour
705 of failure, which influences slope stability as a whole.

706

707 **Acknowledgements**

708 The authors gratefully acknowledge the continued support for this research from ICL
709 Fertilizers (UK) Ltd. We also thank Sam Waugh, Emma Vann Jones, Heather Bell, Simon
710 Varley and Zuzanna Swirad for help with the collection of field data.

711

712 **References**

- 713 Abellán, A., Calvet, J., Vilaplana, J.M., Blanchard, J., 2010. Detection and spatial prediction
714 of rockfalls by means of terrestrial laser scanner monitoring. *Geomorphology* 119, 162–
715 171. doi:10.1016/j.geomorph.2010.03.016
- 716 Attewell, P.B., Farmer, I.W., 1973. Fatigue behaviour of rock. *International Journal of Rock*
717 *Mechanics and Mining Sciences & Geomechanics Abstracts* 1–9.
- 718 Augustinus, P.C., 1992. The influence of rock mass strength on glacial valley cross-profile
719 morphometry: A case study from the Southern Alps, New Zealand. *Earth Surface*
720 *Processes and Landforms* 17, 39–51.
- 721 Barlow, J., Lim, M., Rosser, N., Petley, D., Brain, M., Norman, E., Geer, M., 2012. Modeling
722 cliff erosion using negative power law scaling of rockfalls. *Geomorphology* 139–140,
723 416–424. doi:10.1016/j.geomorph.2011.11.006
- 724 Barton, N., 1974. Estimating the shear strength of rock joints, in: *Proceedings of the 3rd*
725 *Congress of International Society of Rock Mechanics. Advances in Rock Mechanics.*

726 Denver, pp. 219–220.

727 Bonilla-Sierra, V., Scholtès, L., Victor, F., Elmouttie, M., 2015. DEM analysis of rock bridges
728 and the contribution to rock slope stability in the case of translational sliding failures.
729 International Journal of Rock Mechanics and Mining Sciences 80, 67–78.
730 doi:10.1016/j.ijrmms.2015.09.008

731 Brain, M.J., Rosser, N.J., Norman, E.C., Petley, D.N., 2014. Are microseismic ground
732 displacements a significant geomorphic agent? *Geomorphology* 207, 161–173.
733 doi:10.1016/j.geomorph.2013.11.002

734 Brideau, M., Yan, M., Stead, D., 2009. The role of tectonic damage and brittle rock fracture
735 in the development of large rock slope failures. *Geomorphology* 103, 30–49.
736 doi:10.1016/j.geomorph.2008.04.010

737 Bruthans, J., Soukup, J., Vaculikova, J., Filippi, M., Schweigstillova, J., Mayo, A.L., Masin,
738 D., Kletetschka, G., Rihosek, J., 2014. Sandstone landforms shaped by negative
739 feedback between stress and erosion. *Nature Geosci* 7, 597–601.

740 Clarke, B.A., Burbank, D.W., 2011. Quantifying bedrock-fracture patterns within the shallow
741 subsurface: Implications for rock mass strength, bedrock landslides, and erodibility.
742 *Journal of Geophysical Research: Earth Surface* 116. doi:10.1029/2011JF001987

743 Clarke, B.A., Burbank, D.W., 2010. Bedrock fracturing, threshold hillslopes, and limits to the
744 magnitude of bedrock landslides. *Earth and Planetary Science Letters* 297, 577–586.
745 doi:10.1016/j.epsl.2010.07.011

746 Collins, B.D., Stock, G.M., 2016. Rockfall triggering by cyclic thermal stressing of exfoliation
747 fractures. *Nature Geoscience*. doi:10.1038/NGEO2686

748 Cruden, D.M., 1974. The static fatigue of brittle rock under uniaxial compression.
749 *International Journal of Rock Mechanics and Mining Sciences & Geomechanics* 11, 67–
750 73.

751 de Vilder, S.J., Rosser, N.J., Brain, M.J., Vann Jones, E.. C., 2017. Forensic rockfall scar
752 analysis: Development of a mechanically correct model of rockfall failure. 3rd North
753 American Symposium on Landslides 829–839.

754 Dunning, S.A., Massey, C.I., Rosser, N.J., 2009. Structural and geomorphological features
755 of landslides in the Bhutan Himalaya derived from Terrestrial Laser Scanning.
756 *Geomorphology* 103, 17–29. doi:10.1016/j.geomorph.2008.04.013

757 Dussauge, C., Grasso, J.-R., Helmstetter, A., 2003. Statistical analysis of rockfall volume
758 distributions: Implications for rockfall dynamics. *Journal of Geophysical Research (Solid*
759 *Earth)* 108, ETG2.1--ETG2.11. doi:10.1029/2001JB000650

760 Eberhardt, E., Stead, D., Coggan, J.S., 2004. Numerical analysis of initiation and
761 progressive failure in natural rock slopes—the 1991 Randa rockslide. *International*
762 *Journal of Rock Mechanics and Mining Sciences* 41, 69–87. doi:10.1016/S1365-
763 1609(03)00076-5

764 Elmo, D., Clayton, C., Rogers, S., Beddoes, R., Greer, S., 2011. Numerical Simulations of
765 Potential Rock Bridge Failure within a Naturally Fractured Rock Mass, in: *Slope*
766 *Stability 2011: International Symposium on Rock Slope Stability in Open Pit Mining and*
767 *Civil Engineering*. pp. 1–13.

768 Fell, R., Corominas, J., Bonnard, C., Cascini, L., Leroi, E., Savage, W.Z., 2008. Guidelines
769 for landslide susceptibility, hazard and risk zoning for land-use planning. *Engineering*
770 *Geology* 102, 99–111. doi:10.1016/j.enggeo.2008.03.014

771 Frayssines, M., Hantz, D., 2009. Modelling and back-analysing failures in steep limestone
772 cliffs. *International Journal of Rock Mechanics and Mining Sciences* 46, 1115–1123.
773 doi:10.1016/j.ijrmms.2009.06.003

774 Frayssines, M., Hantz, D., 2006. Failure mechanisms and triggering factors in calcareous
775 cliffs of the Subalpine Ranges (French Alps). *Engineering Geology* 86, 256–270.
776 doi:10.1016/j.enggeo.2006.05.009

777 Gerber, E., Schiedegger, A.E., 1969. Stress induced weathering of rock masses. *Eclogae*
778 *geol Helv* 62, 401–415.

779 Gischtig, V., Amann, F., Moore, J.R., Loew, S., Eisenbeiss, H., Stempfhuber, W., 2011.
780 Composite rock slope kinematics at the current Randa instability, Switzerland, based
781 on remote sensing and numerical modeling. *Engineering Geology* 118, 37–53.

782 doi:10.1016/j.enggeo.2010.11.006

783 Gischig, V.S., Moore, J.R., Evans, K., Amann, F., Loew, S., 2011. Thermomechanical
784 forcing of deep rock slope deformation : 1 . Conceptual study of a simplified slope.
785 Journal of Geophysical Research 116, 1–18. doi:10.1029/2011JF002006

786 Goodman, R.E., Shi, G., 1985. Block Theory and its Application to Rock Engineering.
787 Prentice-Hall Inc, New Jersey. doi:10.1016/0013-7952(88)90010-5

788 Grøneng, G., Nilsen, B., Sandven, R., 2009. Shear strength estimation for a ϕ -knes sliding
789 area in western Norway. International Journal of Rock Mechanics and Mining Sciences
790 46, 479–488. doi:10.1016/j.ijrmms.2008.10.006

791 Gunzburger, Y., Merrien-Soukatchoff, V., Guglielmi, Y., 2005. Influence of daily surface
792 temperature fluctuations on rock slope stability: a case study of the Rochers de
793 Valabres slope (France). International Journal of Rock Mechanics and Mining Sciences
794 42, 331–349.

795 Hibbeler, R.C., 2010. Engineering Mechanics Statics, 12th ed. Pearson, Singapore.

796 Hoek, E., Brown, E., 1997. Practical estimates of rock mass strength. International Journal
797 of Rock Mechanics and Mining Sciences 34, 1165–1186. doi:10.1016/S1365-
798 1609(97)80069-X

799 Huang, Q., Angelier, J., 1989. Fracture spacing and its relation to bed thickness. Geological
800 Magazine 126, 355–362. doi:10.1017/S0016756800006555

801 ISRM, 2015. The ISRM Suggested Methods for Rock Characterization, Testing and
802 Monitoring:2007-2014, 1st ed. Springer International Publishing.

803 Jennings, J.E., 1970. A mathematical theory for the calculation of the stability of open cast
804 mines, in: Van Rensburg, P. (Ed.), Planning Open Pit Mines: Proceedings of the
805 Symposium on the Theoretical Background to the Planning of Open Pit Mines with
806 Special Reference to Slope Stability. Balkema (A.A.), Johannesburg, pp. 87–102.

807 Karami, A., Greer, S., Beddoes, R., 2007. Numerical assessment of step-path failure of
808 northwest wall of A154 Pit, Diavik Diamond Mines, in: Potvin, Y. (Ed.), Slope Stability
809 2007 : Proceedings of the 2007 International Symposium on Rock Slope Stability in

810 Open Pit Mining and Civil Engineering. Australian centre for geomechanics, Perth, pp.
811 293–305.

812 Kemeny, J., 2003. The time-dependent reduction of sliding cohesion due to rock bridges
813 along discontinuities: A fracture mechanics approach. *Rock Mechanics and Rock*
814 *Engineering* 36, 27–38. doi:10.1007/s00603-002-0032-2

815 Koons, P.O., Upton, P., Barker, A.D., 2012. The influence of mechanical properties on the
816 link between tectonic and topographic evolution. *Geomorphology* 137, 168–180.
817 doi:10.1016/j.geomorph.2010.11.012

818 Kranz, R., 1983. Microcracks in rocks: a review. *Tectonophysics* 100, 449–480.

819 Kromer, R.A., Hutchinson, D.J., Lato, M.J., Gauthier, D., Edwards, T., 2015. Identifying rock
820 slope failure precursors using LiDAR for transportation corridor hazard management.
821 *Engineering Geology* 195, 93–103. doi:10.1016/j.enggeo.2015.05.012

822 Ladeira, F.L., Price, N.J., 1981. Relationship between fracture spacing and bed thickness.
823 *Journal of Structural Geology* 3, 179–183. doi:10.1016/0191-8141(81)90013-4

824 Leroueil, S., 2001. Natural slopes and cuts: movement and failure mechanisms.
825 *Geotechnique* 51, 197–243.

826 Lévy, C., Baillet, L., Jongmans, D., Mouro, P., Hantz, D., 2010. Dynamic response of the
827 Chamousset rock column (Western Alps , France). *Journal of Geophysical Research*
828 115, 1–13. doi:10.1029/2009JF001606

829 Li, Y., Onasch, C.M., Guo, Y., 2008. GIS-based detection of grain boundaries. *Journal of*
830 *Structural Geology* 30, 431–443. doi:10.1016/j.jsg.2007.12.007

831 Lim, M., Rosser, N.J., Allison, R.J., Petley, D.N., 2010. Erosional processes in the hard rock
832 coastal cliffs at Staithes, North Yorkshire. *Geomorphology* 114, 12–21.
833 doi:10.1016/j.geomorph.2009.02.011

834 Malamud, B.D., Turcotte, D.L., Guzzetti, F., Reichenbach, P., 2004. Landslide inventories
835 and their statistical properties. *Earth Surface Processes and Landforms* 29, 687–711.
836 doi:10.1002/esp.1064

837 Martel, S.J., 2017. Progress in understanding sheeting joints over the past two centuries.

838 Journal of Structural Geology 94, 68–86. doi:10.1016/j.jsg.2016.11.003

839 Matasci, B., Jaboyedoff, M., Loye, A., Pedrazzini, A., Derron, M.H., Pedrozzi, G., 2015.

840 Impacts of fracturing patterns on the rockfall susceptibility and erosion rate of stratified

841 limestone. *Geomorphology* 241, 83–97. doi:10.1016/j.geomorph.2015.03.037

842 McConaughy, D.T., Engelder, T., 2001. Joint initiation in bedded clastic rocks. *Journal of*

843 *Structural Geology* 23, 203–221. doi:10.1016/S0191-8141(00)00091-2

844 Moore, J.R., Sanders, J.W., Dietrich, W.E., Glaser, S.D., 2009. Influence of rock mass

845 strength on the erosion rate of alpine cliffs. *Earth Surface Processes and Landforms* 34,

846 1339–1352. doi:10.1002/esp.1821

847 Narr, W., Suppe, J., 1991. Joint spacing in sedimentary rocks. *Journal of Structural Geology*

848 13, 1037–1048. doi:10.1016/0191-8141(91)90055-N

849 Otsu, N., 1979. A threshold selection method from gray-level histograms. *IEEE transactions*

850 *on systems, man, and cybernetics* SMC-9, 62–66.

851 Paronuzzi, P., Bolla, A., Rigo, E., 2016. 3D Stress – Strain Analysis of a Failed Limestone

852 Wedge Influenced by an Intact Rock Bridge. *Rock Mechanics and Rock Engineering*

853 49, 3223–3242. doi:10.1007/s00603-016-0963-7

854 Paronuzzi, P., Sera, W., 2009. Stress state analysis of a collapsed overhanging rock slab : A

855 case study. *Engineering Geology* 108, 65–75. doi:10.1016/j.enggeo.2009.06.019

856 Pollard, D.D., Aydin, A., 1988. Progress in understanding jointing over the past century.

857 *Geological Society of America Bulletin* 100, 1181–1204. doi:10.1130/0016-

858 7606(1988)100<1181

859 Priest, S.D., 1993. *Discontinuity Analysis for Rock Engineering*. Springer Netherlands.

860 doi:10.1007/978-94-011-1498-1

861 Rawson, P.F., Wright, J.K., 2000. *The Yorkshire Coast*, 3rd ed, Geologists' Association

862 Guide. Geologists' Association, Burlington House, Piccadilly, London.

863 Rosser, N., Lim, M., Petley, D., Dunning, S., Allison, R., 2007. Patterns of precursory rockfall

864 prior to slope failure. *Journal of Geophysical Research* 112. doi:10.1029/2006JF000642

865 Rosser, N.J., Brain, M.J., Petley, D.N., Lim, M., Norman, E.C., 2013. Coastline retreat via

866 progressive failure of rocky coastal cliffs. *Geology* 41, 939–942. doi:10.1130/G34371.1

867 Rosser, N.J., Petley, D.N., Lim, M., Dunning, S.A., Allison, R.J., 2005. Terrestrial laser
868 scanning for monitoring the process of hard rock coastal cliff erosion. *Quarterly Journal*
869 *of Engineering Geology and Hydrogeology* 38, 363–375. doi:10.1144/1470-9236/05-
870 008

871 Scavia, C., 1995. A method for the study of crack propagation in rock structures.
872 *Geotechnique* 45, 447–463.

873 Scavia, C., 1990. Fracture mechanics approach to stability analysis of rock slopes.
874 *Engineering Fracture Mechanics* 35, 899–910.

875 Scavia, C., Castelli, M., 1996. Analysis of the propagation of natural discontinuities in rock
876 bridges, in: *Eurock*. pp. 445–451.

877 Selby, M.J., 1982. Rock mass strength and the form of some inselbergs in the central Namib
878 Desert. *Earth Surface Processes and Landforms* 7, 489–497.

879 Selby, M.J., 1980. A rock mass strength classification for geomorphic purposes: with tests
880 from Antarctica and New Zealand. *Zeitschrift für Geomorphologie* 24, 31–51.

881 Silverman, B.W., 1986. *Density estimation for statistics and data analysis*. Chapman and
882 Hall, New York.

883 Stead, D., Eberhardt, E., Coggan, J.S., 2006. Developments in the characterization of
884 complex rock slope deformation and failure using numerical modelling techniques.
885 *Engineering Geology* 83, 217–235. doi:10.1016/j.enggeo.2005.06.033

886 Stock, G.M., Bawden, G.W., Green, J.K., Hanson, E., Downing, G., Collins, B.D., Bond, S.,
887 Leslar, M., 2011. High-resolution three-dimensional imaging and analysis of rock falls in
888 Yosemite Valley, California. *Geosphere* 7, 573–581.

889 Stock, G.M., Martel, S.J., Collins, B.D., Harp, E.L., 2012. Progressive failure of sheeted rock
890 slopes: the 2009-2010 Rhombus Wall rock falls in Yosemite Valley, California, USA.
891 *Earth Surface Processes and Landforms* 37, 546–561. doi:10.1002/esp.3192

892 Sturzenegger, M., Stead, D., 2012. The Palliser Rockslide , Canadian Rocky Mountains :
893 Characterization and modeling of a stepped failure surface. *Geomorphology* 138, 145–

894 161. doi:10.1016/j.geomorph.2011.09.001

895 Sturzenegger, M., Stead, D., 2009. Close-range terrestrial digital photogrammetry and
896 terrestrial laser scanning for discontinuity characterization on rock cuts. *Engineering*
897 *Geology* 106, 163–182. doi:10.1016/j.enggeo.2009.03.004

898 Tuckey, Z., Stead, D., 2016. Improvements to field and remote sensing methods for mapping
899 discontinuity persistence and intact rock bridges in rock slopes. *Engineering Geology*
900 208, 136–153. doi:10.1016/j.enggeo.2016.05.001

901 Viles, H.A., 2013. Linking weathering and rock slope instability: non-linear perspectives.
902 *Earth Surface Processes and Landforms* 38, 62–70. doi:10.1002/esp.3294

903 Wyllie, D.C., Mah, C.W., 2004. *Rock Slope Engineering: Civil and Mining*, 4th ed. Taylor and
904 Francis Group, New York.

905